Science Advances

AAAS

advances.sciencemag.org/cgi/content/full/3/4/e1603224/DC1

Supplementary Materials for

Genuine binding energy of the hydrated electron

David Luckhaus, Yo-ichi Yamamoto, Toshinori Suzuki, Ruth Signorell

Published 28 April 2017, *Sci. Adv.* **3**, e1603224 (2017)
DOI: 10.1126/sciadv.1603224

This PDF file includes:

- Supplementary Text
- Supplementary Materials and Methods
- section S1. Experimental values for the VBE of the bulk hydrated electron
- section S2. Description of scattering calculations
- section S3. Description of experimental setup
- section S4. Additional eKE distributions
- section S5. Sensitivity of eKE distributions to scattering parameters
- section S6. Additional electron binding energy spectra
- section S7. Probing depth and surface sensitivity
- section S8. Photoelectron angular distribution
- table S1. Previously reported values of the VBEs for the bulk hydrated electron.
- fig. S1. Experimental VBEs by Yamamoto *et al.* (*8*).
- fig. S2. Light intensity distribution in the liquid microjet.
- fig. S3. Integral scattering cross sections for electrons in water as a function of the eKE as derived by Signorell *et al.* and Michaud *et al.* (*35*, *39*).
- fig. S4. Scheme of the experimental setup.
- fig. S5. Direct comparison of the experimental and calculated photoelectron kinetic energy distributions from Fig. 2 for all probe energies $h\nu$.
- fig. S6. The influence of scattering on the eKE distributions.
- fig. S7. Sensitivity of eKE distributions to an increase in the inelastic mean free path of +40%, which corresponds to the upper uncertainty limit of the IMFP (*35*).
- fig S8. Sensitivity of eKE distributions to a change in the angular distribution of the inelastic scattering events (section S2).
- fig. S9. Experimental eBE spectra for the different photon energies between $3.6\ \text{eV} \leq h\nu \leq 13.6\ \text{eV}$.
- fig. S10. Uncertainty of the $\text{eBE}^{(g)}$ spectrum.

- fig. S11. Fraction of the total electron intensity that originates from cylindrical shells of various thickness for photon energies 3.6 eV ≤ $h\nu$ ≤ 13.6 eV and for a photon energy $h\nu$ = 38.7 eV (red, dashed line) (*6*).
- fig. S12. Surface contribution to the eBE spectra for (A) $h\nu$ = 3.6 eV and (B) $h\nu$ = 5.8 eV.
- fig. S13. Calculated angle-dependent liquid jet photoelectron spectra for different ionization laser polarization directions 0° ≤ θ ≤ 90° (section S2 and fig. S4) and a photon energy of $h\nu$ = 4.8 eV (*23*).
- fig. S14. Calculated velocity map photoelectron image for hydrated electrons in an anion cluster with ~50 H_2O molecules for a genuine anisotropy parameter $\beta^{(g)}$ = 0.6 and a photon energy of $h\nu$ = 3.1 eV (*45*).
- References (*47–57*)

Supplementary Text

section S1. Experimental values for the VBE of the bulk hydrated electron

Table S1 summarizes the reported experimental values for the vertical electron binding energy (VBE) of the bulk hydrated electron retrieved from liquid microjet photoelectron spectra, which were recorded at different ionization (probe) energies *hν*. It is assumed that the ground state hydrated electron was probed. The VBEs are derived from the most probable electron kinetic energy eKE^{max} (position of maxima in the experimental eKE distributions) using the relation $\mathrm{VBE} = h\nu - \mathrm{eKE}^{(\max)}$. In addition to liquid microjet data, the table contains an extrapolated bulk value for the VBE obtained from anion water cluster studies (*20*, *21*, *47*). The latest theoretical work by Herbert *et al.* (*13*) suggests theoretical VBEs in the range 3.3–3.6 eV. See ref. (*13*) for previous theoretical values.

table S1. Previously reported values of the VBEs for the bulk hydrated electron.

Previously reported values of the vertical electron binding energies (VBE) for the bulk hydrated electron. *hν* and *λ* are the ionization (probe) laser energy and wavelength, respectively.

VBE / eV	***hν* / eV**	***λ* / nm**	**Ref.**
3.3	38.7	32.0	(*6*)
3.6 ± 0.1	4.7 / 5.8	266 / 213	(*7*)
3.27 ± 0.10	4.8	260	(*5*)
3.4	4.7	266	(*27*)
3.42(6)	4.8	260	(*48*)
3.4	4.7	266	(*28*)
3.7 eV without suggested scattering correction of –0.5 eV	13.6	91.2	(*8*)
3.2 eV with suggested scattering correction of –0.5 eV	13.6	91.2	(*8*)
4.5	5.8	215	(*8*)

4.2	5.6	220	(*8*)
3.9	5.4	230	(*8*)
4.1	5.2	240	(*8*)
3.9	5.0	250	(*8*)
3.8	4.8	260	(*8*)
3.7	4.6	270	(*8*)
3.6	4.4	280	(*8*)
3.6	4.1	300	(*8*)
3.5	3.9	320	(*8*)
3.3	3.6	340	(*8*)
3.6 3.3 ~3.9 anion cluster extrapolations	–	–	(*47*) (*20*) (*21*)

Figure S1 shows the evolution of the experimental VBEs from ref. (*8*) as a function of *h*ν. The genuine vertical binding energy $VBE^{(g)}$ (dashed line, this work) is obscured in the experimental spectra by contributions from electron scattering and limited photon energy of the ionization laser.

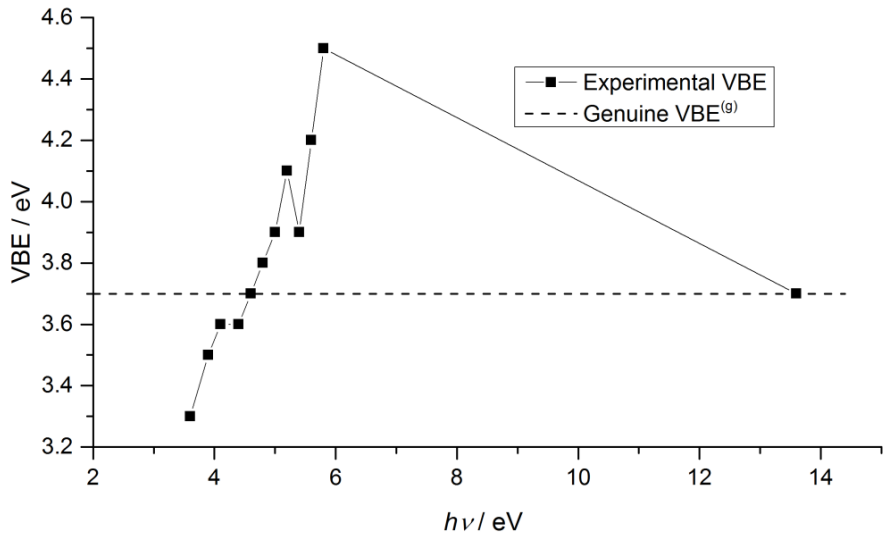

fig. S1. Experimental VBEs by Yamamoto *et al.* (*8*). Horizontal dashed line: Genuine vertical binding energy $VBE^{(g)}$ as extracted from scattering simulations in the present work.

Supplementary Materials and Methods

section S2. Description of scattering calculations

The modeling of the photoelectron spectra of the hydrated electron consist of the following three parts which are explained in more detail below: i) The interaction of the liquid jet with the ionizing radiation *h*ν and the probability of forming quasi-free electrons in the conduction band by ionization of the hydrated electron e_{aq}^- at each point in the microjet. ii) The transport of the electrons from the point of origin (ionization) to the liquid jet surface and the escape from the surface into vacuum. iii) The collection of photoelectrons mimicking the experimental collection geometry. The computer implementation of the model is based on a Monte-Carlo solution of the transport equations. Small overall yields (typically a few per cent) require a large number of Monte-Carlo trajectories to obtain statisfactory statistics. While a few million trajectories suffice for low resolution survey eKE spectra, the simulation of a detailed angle resolved spectrum requires up to a billion trajectories. This becomes possible with a highly parallel computer program which also allows the refinement of model parameters – here the genuine $eBE^{(g)}$ spectrum – using a grid search algorithm.

(i) The probability to generate a quasi-free electron at a certain point in the liquid jet is proportional to the local light intensity of the ionizing radiation *h*ν. The electric field inside the liquid jet is calculated from Maxwell's equations for plane-wave irradiation of a cylinder of 5 μm radius and infinite length (liquid microjet, fig. S4) using the wavelength-dependent complex index of refraction of pure water (*49*). Note that the jet diameter in the experiment is estimated to lie between 10 and 15 μm. We have tested that the results of our calculations are independent of the jet diameter in that range. The propagation and polarization direction of the linearly polarized light are identical to the experiment (fig. S4). Maxwell's equations were solved numerically using a finite-difference time-domain (FDTD) code (*50*). Figure S2 shows two typical internal cross sectional intensity distributions for *h*ν = 5.8 eV (A) and 13.6 eV (B). The internal intensities for *h*ν ≤ 5.8 eV look very similar to the case for *h*ν = 5.8 eV. At *h*ν = 5.8 eV, the light illuminates the liquid jet almost completely with increasing focusing effects in propagation direction (*35*) because water does not absorb UV light (imaginary refractive index $k \approx 0$). In the VUV (*h*ν = 13.6 eV), by

contrast, light is strongly absorbed (k = 0.49) by the liquid jet so that only the outermost liquid layer with a thickness of ~ 15 nm is illuminated by the light. The genuine binding energy spectrum ($eBE^{(g)}$) is retrieved from a common, global fit to all eleven photoelectron spectra recorded between $h\nu$ = 3.6 and 5.8 eV (Fig. 1A) using the electron scattering model described in the following. The experimental 13.6 eV spectrum is not used in the fit because of its high noise level (Fig. 2A, fig. S5). The genuine photoelectron angular distribution ($PAD^{(g)}$) and the corresponding anisotropy parameter $\beta^{(g)}$ are obtained from a comparison of scattering calculations with the experimental spectra in Fig. 4d in ref. (*23*).

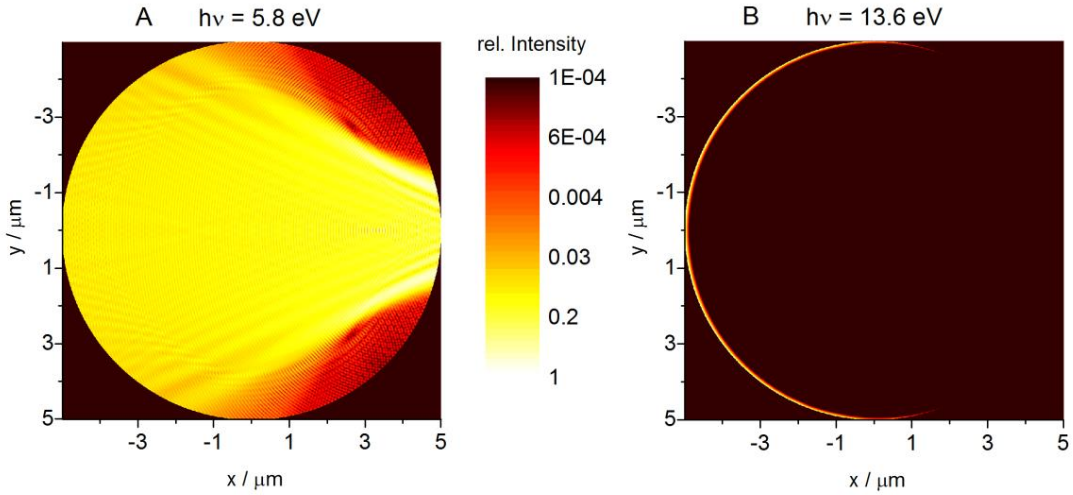

fig. S2. Light intensity distribution in the liquid microjet.

Color map of the internal light intensity (square of the internal electric field) in the water microjet for ionizing radiation of $h\nu$ = 5.8 eV (**A**) and 13.6 eV (**B**), respectively. Shown are cross sectional areas of the microjet. The light propagates in positive x-direction and is linearly-polarized in y-direction.

(ii) The probabilistic electron transport model is formulated as a random walk with an exponential distribution of step lengths. The mean step length, i.e. the electron mean free path MFP(E), depends on the instantaneous kinetic energy E of the electron and is given by $\mathrm{MFP}(E) = \dfrac{1}{\rho\,\sigma_{\mathrm{tot}}(E)}$, where ρ is the number density of scatterers (water molecules) and $\sigma_{\mathrm{tot}}(E)$ is the total scattering cross section. The different scattering

events are described by differential scattering cross sections (DCS) $\sigma\left(E,\Delta_E,\Omega\right)$ for energy loss Δ_E and the deflection angle Ω of the electron. $\sigma\left(E,\Delta_E,\Omega\right)$ is written as the sum of contributions from elastic (i. e. $\Delta_E = 0$) and different types of inelastic scattering (inelastic electron-phonon, electron-vibron, dissociative electron attachment, electron-electron scattering). The total cross section is given by $\sigma_{\text{tot}}\left(E\right) = \iint \sigma\left(E,\Delta_E,\Omega\right) d\Delta_E\, d\Omega$. The DCS used for the present study are taken from ref. (*35*) for excitation energies below 6 eV, which were determined from photoemission studies of liquid water droplets. Note that these data are independent of any of the present experimental liquid jet results. The combination of water droplets and velocity map photoelectron imaging introduced in ref. (*35*) allowed us to determine accurate scattering parameters by exploiting the detailed information contained in the droplet size-dependent photoelectron anisotropies and kinetic energies (*35, 51*). Note that contrary to what is often but wrongly assumed, these supercooled droplets do *not* freeze, but stay liquid on a time-scale orders of magnitude longer than the time scale of the experiment (*35, 52, 53*). For simulations at 13.6 eV and 38.7 eV we have used our droplet data for low kinetic energies and the amorphous ice data of Michaud *et al.* (*39*) for higher kinetic energies, as there is no reason to expect any difference between amorphous ice and liquid water for the electronic scattering processes in this energy range. Figure S3 shows the total integral scattering cross section as a function of kinetic energy together with all individual contributions. Of particular relevance to the present work is the extension of the data range to very low electron kinetic energies as described in detail in ref. (*35*). For the angular dependence of scattering we found the representation proposed by Michaud *et al.* perfectly appropriate also for the liquid (*35*). This models the DCS with an explicit angular dependence given by the sum of a θ-independent term ("isotropic contribution") and a |cos(θ)|-term ("forward contribution"). Our analysis of droplet VMIs (*35*) showed that the effect of elastic scattering is well described by an isotropic contribution alone. We assume a flat bottom of the conduction band so that electrons within the liquid move at a constant potential below the vacuum level. Consequently, they have to overcome the escape barrier V_0 (Fig. 1). The escape barrier is set to V_0 = 1 eV, roughly corresponding to the difference between the onsets of photoemission and photoconduction reported for water ice (*39*). See also refs. (*54, 55*) for further

information on the escape barrier. Electrons with $E < V_0$ are eventually absorbed. The tangential components of the electron's momentum relative to the liquid jet surface is assumed to be conserved when crossing the surface. This leads to a diffraction-like escape condition (Snell's law): The velocity component normal to the liquid jet surface v_n must exceed the escape velocity v_{esc}, i.e. $v_{esc} = \sqrt{\frac{2V_0}{m_e}}$, otherwise, the electron is reflected back into the liquid. m_e is the electron mass. Detailed scattering models similar to the present were suggested in refs. (*35*, *39*).

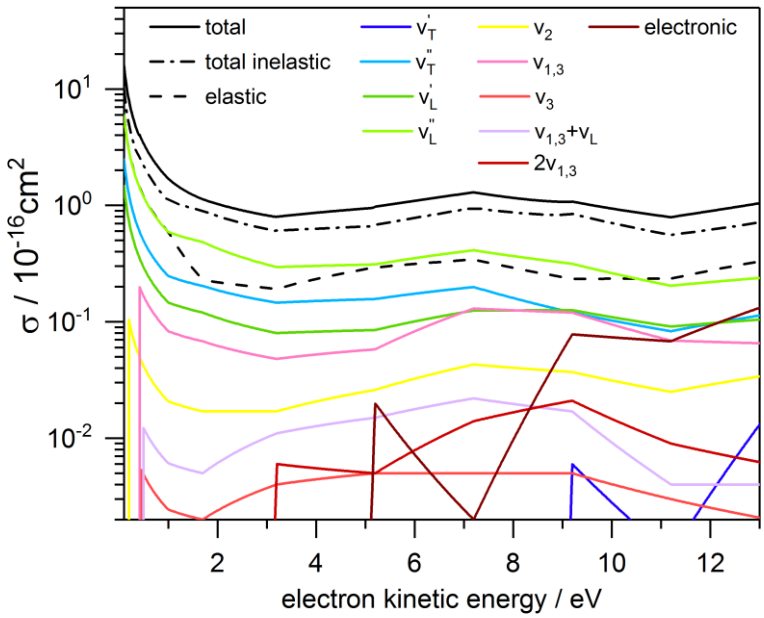

fig. S3. Integral scattering cross sections for electrons in water as a function of the eKE as derived by Signorell *et al.* (*35, 39*). Shown are the total cross section (full black line) together with their elastic (dashed black line) and total inelastic (dash-dotted black line) contributions. The individual inelastic contributions are represented colour-coded and fall into three groups: Intermolecular vibrational (L = librational, T = translational) with energy loss per collision between 0.04 and 0.1 eV, intramolecular vibrational (1,3 = stretch, 2 = bend) with energy losses per collision between 0.2 and 0.9 eV, and electronic scattering (dissociative electron detachment, electronic excitation, impact ionization) with energy losses per collision above 5 eV. The labeling is adopted from Michaud *et al.* (*39*).

(iii) The experimental collection geometry (fig. S4) is used for the calculations of the eKE distribution. In the magnetic bottle spectrometer, all electrons ejected from the liquid microjet are collected. For the simulations of the angle-resolved photoelectron spectra (fig. S13), only the electrons ejected into a small solid angle $\Delta\omega = 9\cdot 10^{-4}$ sr around the electron detection axis ω are collected as for the experimental spectra in ref. (*23*) (fig. S4). $\Delta\omega$ is determined by the detector's surface area (40 mm diameter) and its distance from the point of ionization (1200 mm) (*23*). Angle-resolved photoelectron spectra are simulated by rotating the linear polarization of the ionization laser from $\theta = 0$ to 90°, where θ is the angle between the ionization laser polarization and the electron detection axis (fig. S4). For the description of the PADs, we neglect higher terms and use a single anisotropy parameter β, defined by

$$I(\theta) \propto 1 + \frac{\beta}{2}\left(3\cos^2\theta - 1\right) \qquad \text{(S1)}$$

section S3. Description of experimental setup

The experimental setup (fig. S4) comprises a water microjet, a femtosecond laser system, and a magnetic bottle photoelectron spectrometer (*8, 56*). The laminar liquid jet is discharged from a fused silica capillary (15 μm) into vacuum (0.2 mL/min flow rate). The liquid jet consists either of a 0.1 M aqueous NaI solution (for 3.6 eV ≤ $h\nu$ ≤ 5.8 eV) or a 0.5 M aqueous $K_4[Fe(CN)_6]$ solution (for $h\nu$ = 13.6 eV). Hydrated electrons e_{aq}^- are formed by charge-transfer-to-solvent (CTTS) excitation of the precursor anions (I^- or $Fe(CN)_6^{4-}$) at pump wavelenght λ_{pump} between 215–270 nm. Ionization of e_{aq}^- is induced by the probe laser $h\nu$ after several hundred ps time delay (Eq. (1) main text). All photoelectrons that are emitted from the liquid microjet are collected by a 0.5 mm skimmer located 2 mm from the liquid jet surface. The photoelectrons are detected by the magnetic bottle photoelectron spectrometer with a conical iron cap and a 1.2 m flight tube with a solenoid and a permalloy shield. The spectrometer is specifically designed to obtain a uniform detection efficiency for the entire energy range. The experimental eKE spectra are corrected for the energy-dependent transmission efficiency of the spectrometer, the applied bias voltages, and the potential bias of the liquid jet relative to the entrance skimmer of the spectrometer. The latter amounted to –0.2 V largely due to the streaming potential but possibly

including other contributions (*44*). It was determined experimentally as previously described (*33*). A 1 kHz Ti:sapphire regenerative amplifier (100 fs, 2.3 mJ/pulse) excites two optical parametric amplifiers (OPAs). The outputs (< 240 nm after frequency mixing) of the OPAs are used as pump (215–230 nm; 5 nJ/pulse) and probe (215–340 nm, 10 nJ/pulse) pulse, respectively. For the $K_4[Fe(CN)_6]$ solution, a 270 nm pump pulse and a 90 nm probe pulse (9th harmonic of the Ti:saphire) are used. The linear polarization of the probe laser is either parallel ($\theta = 0°$ for 240–300 nm and 90 nm) or perpendicular ($\theta = 90°$ for 320–340 nm) to the electron detection axis, respectively. For angle-resolved photoelectron spectra, the magnetic bottle spectrometer can be replaced by a time-of-flight spectrometer as described in ref. (*23*). We do not expect any effects of the presence of the electrolyte on the results reported here. We had considered this effect in the context of the experimental determination of scattering parameters from water droplets (*35*), where recorded VMIs were found to be independent of electrolyte concentrations up to 0.1 M. Moreover a computational study by Olivieri *et al.* found no significant difference in the inelastic mean free path between pure water and a 1 M aqueous NaI solution (tenfold the concentration used in the present experiments) (*57*).

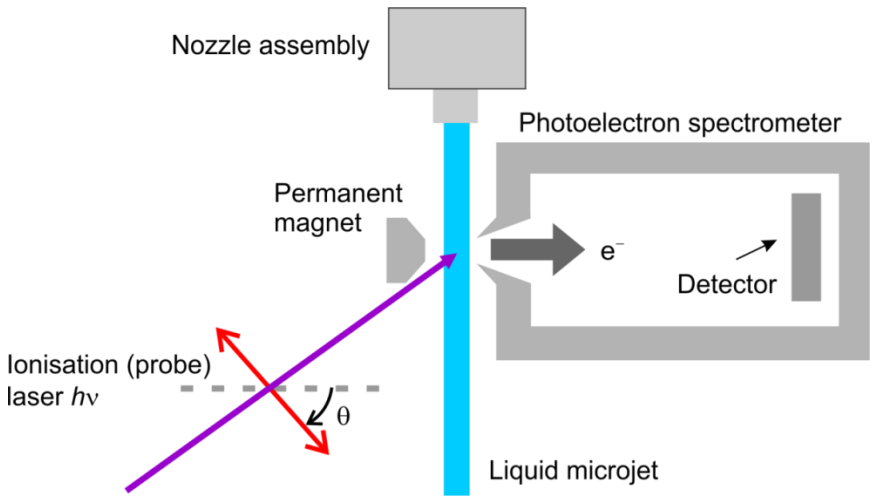

fig. S4. Scheme of the experimental setup. The linearly polarized ionization (probe) laser (violet arrow) propagates from front to back. θ is the angle between the laser polarization and the electron detection axis.

section S4. Additional eKE distributions

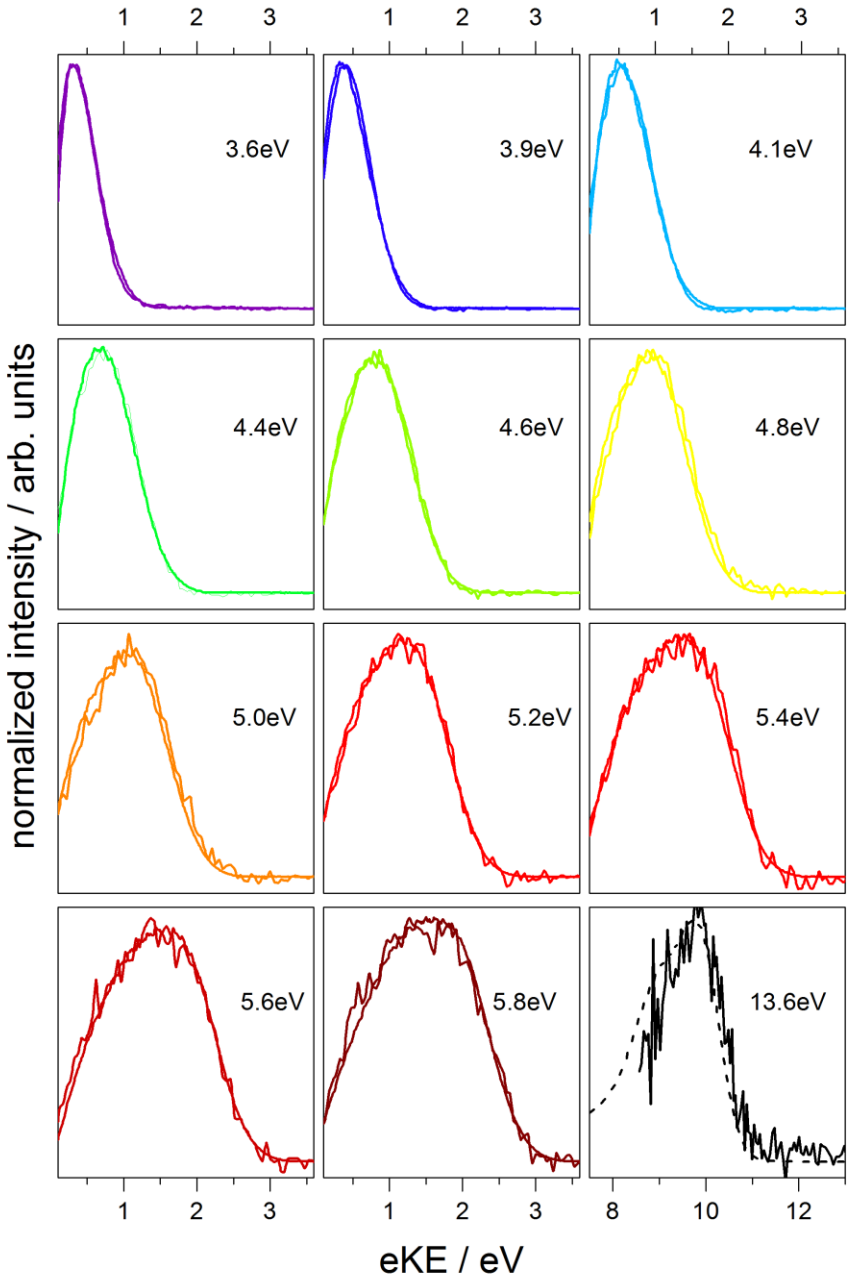

fig. S5. Direct comparison of the experimental and calculated photoelectron kinetic energy distributions from Fig. 2 for all probe energies *hν*.

Direct comparison of the experimental and calculated eKE distribution from Fig. 2 in the main text for all probe energies *hν*. The direct comparison exemplifies the good agreement between experiment and simulation for *hν* ≤ 5.8 eV. The noise in the experimental spectrum recorded at 13.6 eV is comparatively high, in particular at low kinetic energies. This spectrum is a difference spectrum of a $[Fe(CN)_6]^{4-}$ solution with and without solvated electrons in the solution (*11*). The region below ~ 9 eV is

distorted by the strong background signal from $[Fe(CN)_6]^{4-}$ (orders of magnitude higher than the signal from e_{aq}^-) and is thus not shown here. This spectrum was not used for the fit.

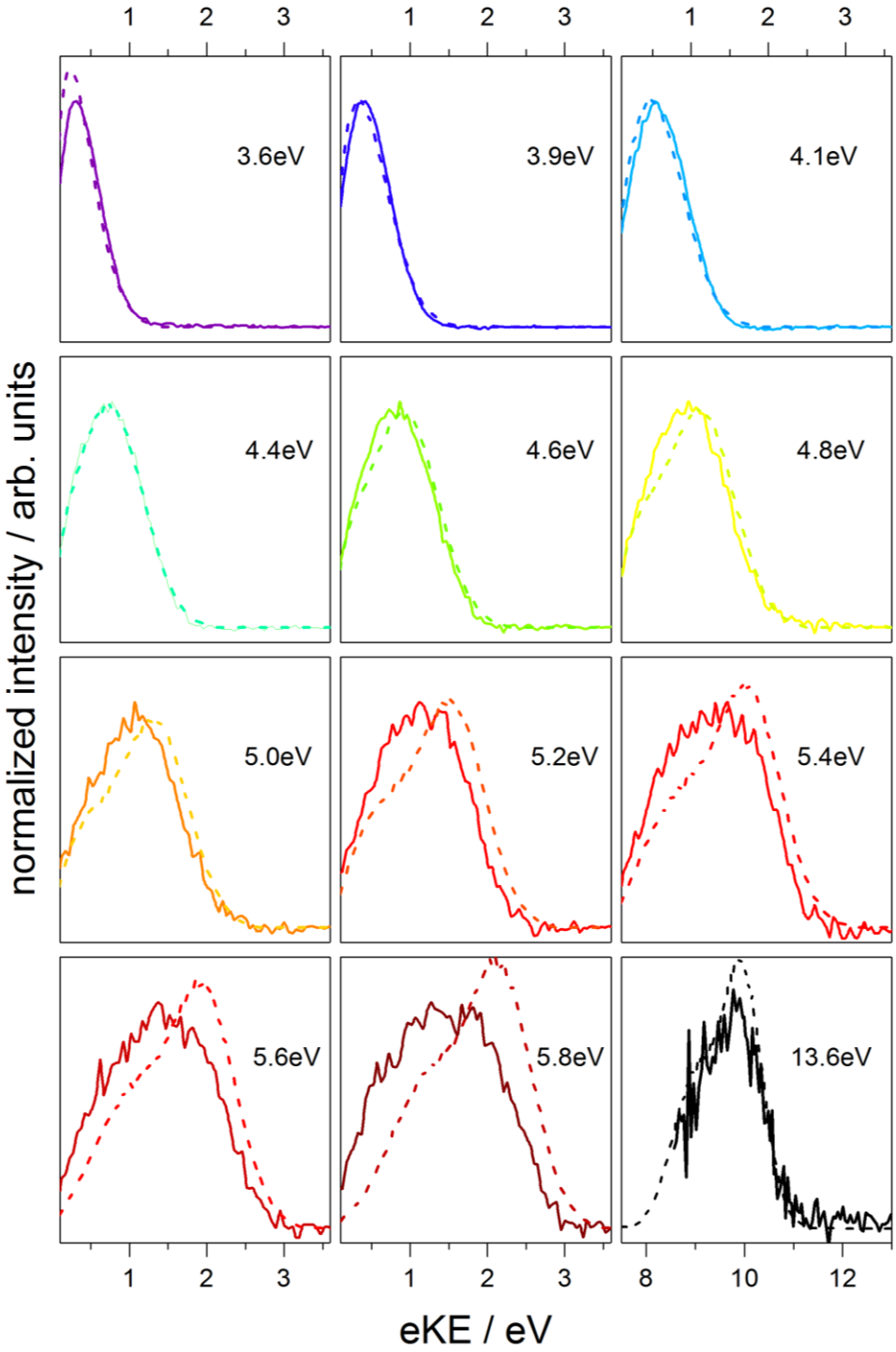

fig. S6. The influence of scattering on the eKE distributions. Full line: Experimental spectra. Dashed line: Simulation without scattering. The simulated

spectra are normalized to the same integrated intensity as the spectra simulated with scattering shown over the same range in fig. S5.

Figure S6 visualizes the importance of scattering to achieve good agreement with the experiment. The seemingly small difference between the simulations with and without scattering around 4 eV is fortuitous. At very low *hv* the eKE is so small that scattering has relatively little influence on the detected eKE spectrum (only electrons that have hardly experienced any scattering can escape from the surface). Here only the lowest energy tail of the $eBE^{(g)}$ is accessible and the measured eBE spectrum is dominated by the energy cut-off. The smooth drop-off towards vanishing eKE (instead of a sharp cut-off) is a result of the escape condition (final escape barrier combined with angular momentum conservation): Please replace by "The lower the kinetic energy of an electron becomes, the more tightly constrained the solid angle is under which it must hit the surface so that its normal velocity component is sufficient to overcome the barrier. With increasing *hv* increasing fractions of the $eBE^{(g)}$ become accessible, which shifts the maximum in the measured eKE spectrum to higher values. At the same time the increasingly important scattering decreases the eKE shifting the measured (apparent) eKE spectrum to lower values. As pointed out in the main text (section: Genuine electron binding energy) the two effects accidentally cancel for photon energies in the range just above 4 eV.

section S5. Sensitivity of eKE distributions to scattering parameters

Figures S7 and S8 show the sensitivity of the calculated eKE distributions to changes in the scattering parameters within their uncertainties (*35*). The two examples demonstrate that corresponding changes in the eKE are insignificant. The same holds for a decrease in the inelastic mean free path (IMFP) of –40% instead of an increase as in fig. S7 as well as for changes in the elastic mean free path (EMFP). The robustness with respect to changes of IMFP and EMFP is a result of the large penetration depth of the ionizing radiation so that the average probability density of nascent photoelectrons is uniform over a depth covering many MFPs. In this regime a change of MFP changes the probing depth while the average number of scattering events an electrons has undergone before it is detected remains similar.

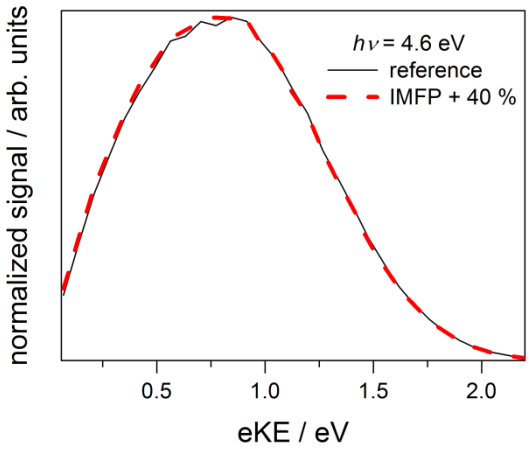

fig. S7. Sensitivity of eKE distributions to an increase in the inelastic mean free path (IMFP) of +40%, which corresponds to the upper uncertainty limit of the IMFP (*35*). Full, black line: original IMFP. Dashed, red line: IMFP increased by +40%.

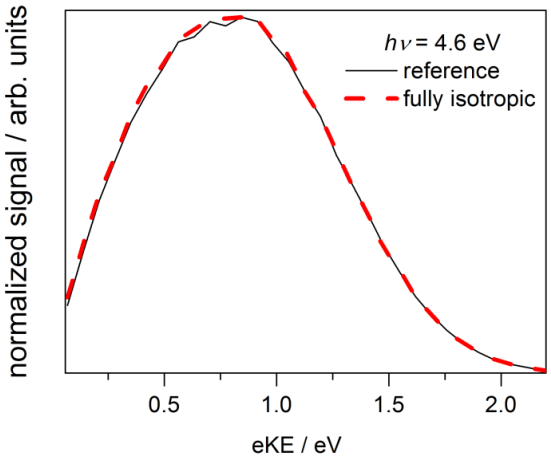

fig S8. Sensitivity of eKE distributions to a change in the angular distribution of the inelastic scattering events (section S2). Full, black line: Original anisotropic scattering cross sections. Dashed, red line: All scattering cross sections assumed to be fully isotropic.

section S6. Additional electron binding energy spectra

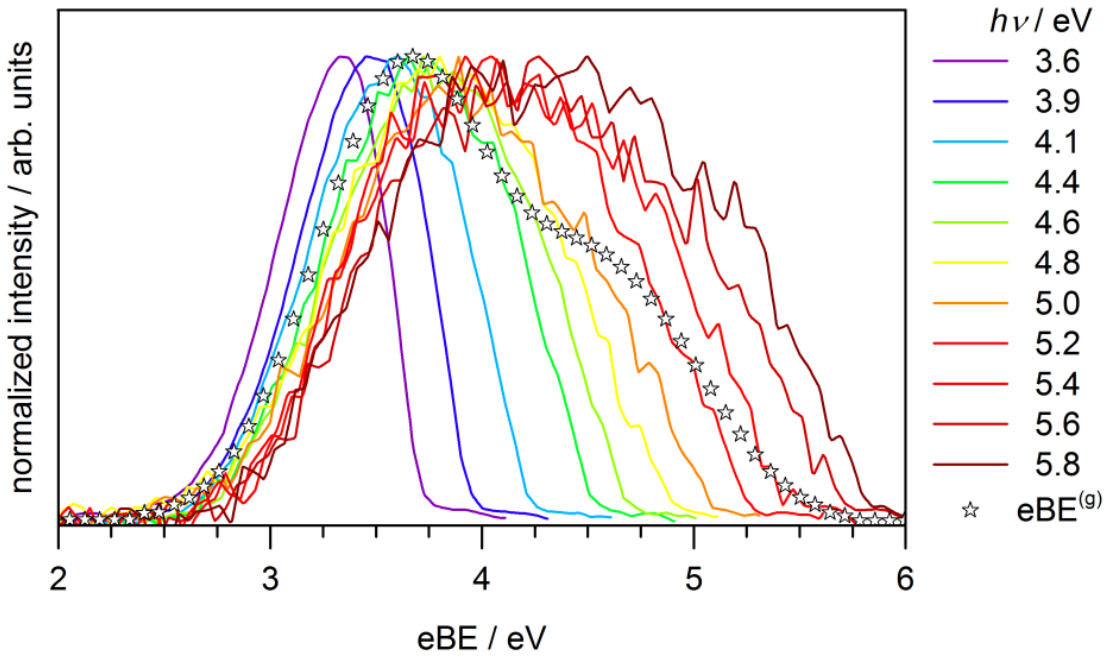

fig. S9. Experimental eBE spectra for the different photon energies between 3.6 eV ≤ *hν* ≤ 13.6 eV. The eBE spectra are identical to the simulations shown in Fig. 3 in the main text. The stars represent the genuine eBE$^{(g)}$ spectrum; i. e. the spectrum devoid of scattering contributions of the electron in the liquid water matrix.

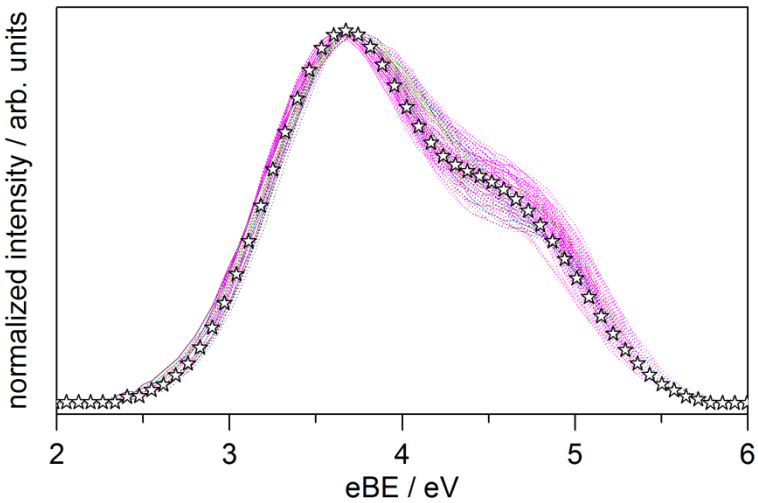

fig. S10. Uncertainty of the eBE$^{(g)}$ spectrum. The dashed red traces represent a random sample of calculated eBE$^{(g)}$ spectra compatible within experimental uncertainties with the spectra shown in fig. S9. The stars represent the best fit result. The low energy flank is well determined within about ± 0.05 eV, while the high energy flank (corresponding to low eKE values) is less tightly constrained by the experimental data. The position of the maximum, however, is only marginally affected by this latter uncertainty resulting in a final value of VBE$^{(g)}$ = 3.7 ± 0.1 eV.

section S7. Probing depth and surface sensitivity

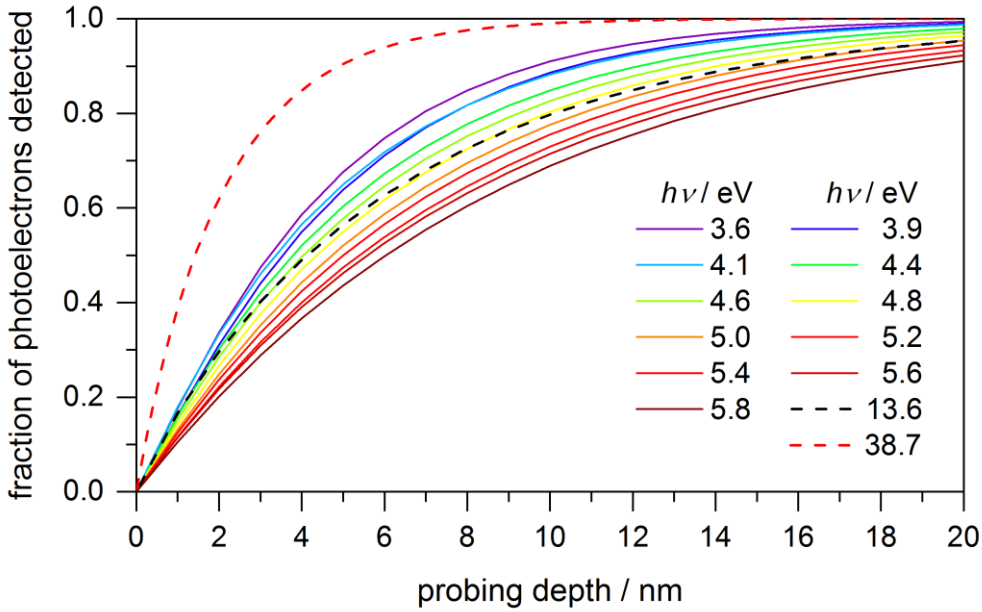

fig. S11. Fraction of the total electron intensity that originates from cylindrical shells of various thickness for photon energies 3.6 eV ≤ *hν* ≤ 13.6 eV and for a photon energy *hν* = 38.7 eV (red, dashed line) (*6*). The probing depth corresponds

the thickness x of the shell (x = 0 nm: liquid jet surface; x = 5 µm: full liquid jet). The probing depths in Fig. 4 in the main text correspond to fractions of 0.63 and 0.80, respectively.

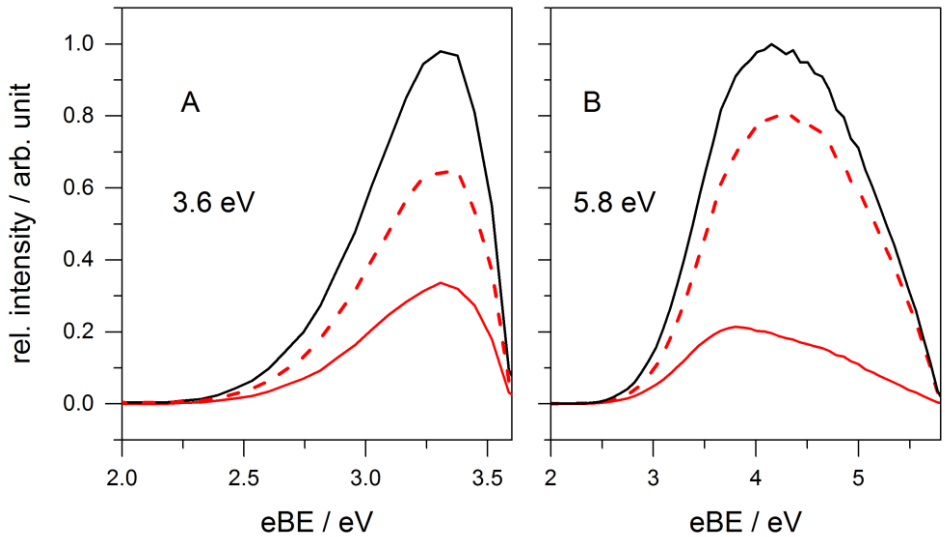

fig. S12. Surface contribution to the eBE spectra for (A) *hν* = 3.6 eV and (B) *hν* = 5.8 eV. Black full line: Total eBE spectrum for the liquid jet. Full red line: Contribution of a 2 nm cylindrical shell to the eBE spectrum. Dashed red line: Contribution of the remaining cylindrical core (liquid jet minus the 2 nm cylindrical shell) to the eBE spectrum. Spectra recorded at photon energies with lower probing depths are more surface sensitive than those recorded at photon energies with higher probing depths (fig. S11). The surface contribution to the total spectrum is thus higher for the *hν* = 3.6 eV spectrum, compared with the *hν* = 5.8 eV spectrum. The comparison of the shell and core spectrum for *hν* = 5.8 eV also reveals the different shape of shell and core spectra as a consequence of electron scattering. The electrons from the shell have undergone fewer scattering events and thus more closely follow the genuine $eBE^{(g)}$ spectrum (open stars in Fig. 3 and fig. S9) than core electrons. Note that this information is lost in the 3.6 eV shell spectrum because of insufficient photon energy.

section S8. Photoelectron angular distribution

Figure S13 shows simulated liquid microjet eBE spectra for *hν* = 4.8 eV and different laser polarization directions $0° \leq \theta \leq 90°$ as described in section S2 and fig. S4. We obtain a similarly small photoemission anisotropy (almost isotropic, $\beta \approx 0$) as for the

liquid jet experiment in Fig. 4d of ref. (*23*) for a genuine anisotropy parameter $\beta^{(g)}$ = 0.6 ± 0.2. The almost complete loss of photoemission anisotropy is caused by scattering in the liquid jet. A genuine anisotropy parameter of $\beta^{(g)}$ = 0.6 ± 0.2 at an eKE ~ 1eV is consistent with an s-like ground state wavefunction of e_{aq}^- and is in agreement with an experimental anisotropy parameter $\beta_{cluster}$ ≈ 0.7 ± 0.1 at an eKE ~ 1eV determined for water anion clusters with ~ 50 H_2O molecules for isomer I in ref. (*45*) (see fig. S14).

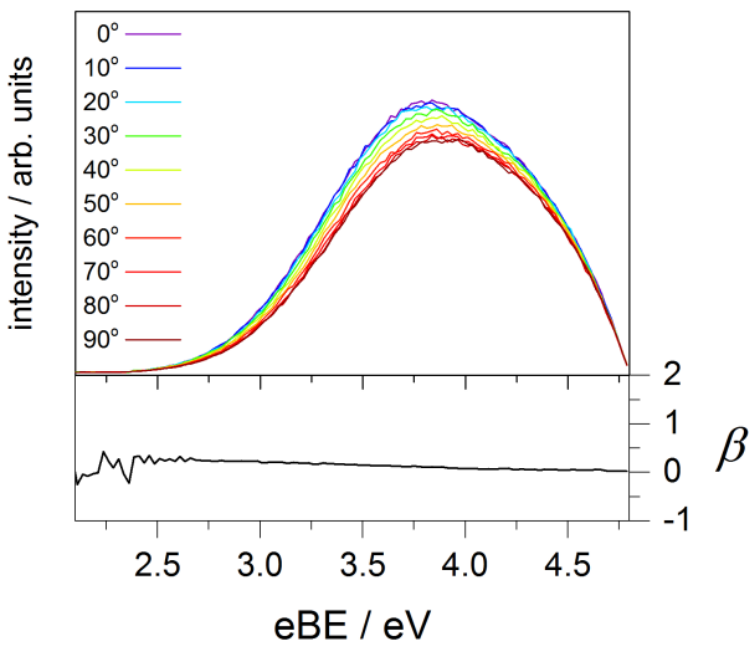

fig. S13. Calculated angle-dependent liquid jet photoelectron spectra for different ionization laser polarization directions 0° ≤ θ ≤ 90° (section S2 and fig. S4) and a photon energy of *hν* = 4.8 eV (*23*). The calculations are for a genuine photoelectron angular distribution PAD$^{(g)}$ with an anisotropy parameter $\beta^{(g)}$ = 0.6. The black trace shows the anisotropy parameter β as derived from eq. (S1). It shows a similarly small photoemission anisotropy (almost isotropic) as the liquid jet experiment in Fig. 4d of ref. (*23*).

Figure S14 shows a calculated velocity map photoelectron image for hydrated electrons in an anion cluster with ~ 50 H_2O molecules for a genuine anisotropy parameter $\beta^{(g)}$ = 0.6 and *hν* = 3.1 eV (*45*). The calculations are equivalent to the

calculation for aerosol droplets in refs. (*35*, *51*). In such small clusters, the eBE of the hydrated electron is much smaller than in the bulk liquid. We simulate its eBE spectrum with a Gaussian centered at 1.8 eV and a FWHM of 0.8 eV in analogy to the spectrum observed in ref. (*45*). The range of eKE values is similar to the 4.8 eV spectrum of the bulk liquid in fig. S13. Using eq. (S1), the velocity map image in fig. S14 yields a cluster anisotropy parameter of $\beta_{\text{cluster}} \approx 0.53$, which remains very close to the genuine value because electron scattering in such small clusters is almost negligible. This value is consistent with the experimental value $\beta_{\text{cluster}} \approx 0.7 \pm 0.1$ for anion clusters with ~ 50 H_2O molecules from ref. (*45*) (see data for isomer I in Fig. 9a in ref. (*45*)).

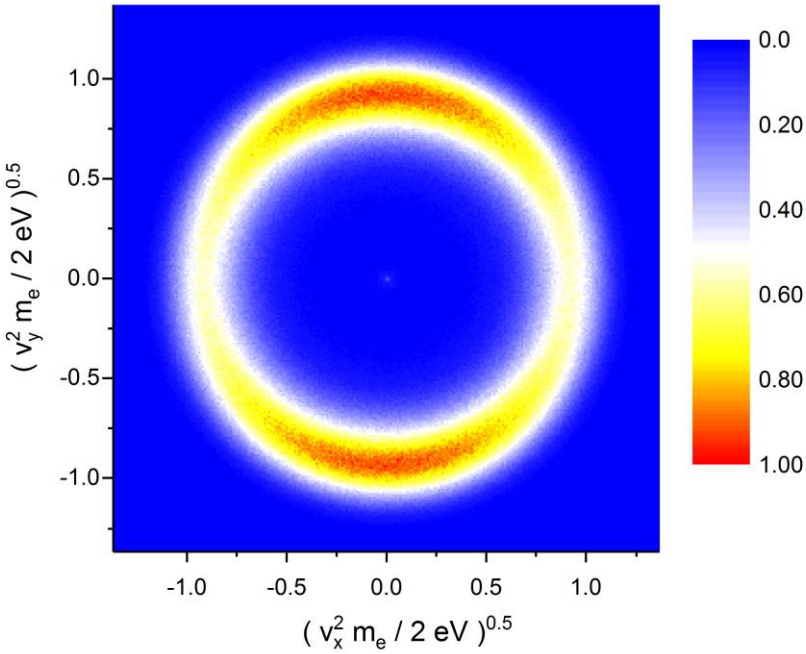

fig. S14. Calculated velocity map photoelectron image for hydrated electrons in an anion cluster with ~50 H2O molecules for a genuine anisotropy parameter $\beta^{(g)}$ = 0.6 and a photon energy of *hν* = 3.1 eV (*45*). The anisotropy parameter for this image is $\beta \approx 0.53$ (eq. (S1)). This value is consistent with the experimental value $\beta_{\text{cluster}} \approx 0.7 \pm 0.1$ for anion clusters with ~50 H_2O molecules from ref. (*45*).